Particle boundary layer above and downstream of an area source: scaling, simulations, and pollen transport

Marcelo Chamecki[1]† and Charles Meneveau[2]

[1] Department of Meteorology, Pennsylvania State University, University Park, PA 16802, USA

[2] Department of Mechanical Engineering and Center for Environmental and Applied Fluid Mechanics, Johns Hopkins University, Baltimore, MD 21218, USA

Dispersion of small particles emitted from an area source at the surface into a fully developed high-Reynolds-number boundary layer flow is studied as a theoretical model for pollen dispersion in the neutral atmospheric boundary layer. The particle plume above the area source is assumed to behave as a particle concentration boundary layer. Boundary layer scaling and the assumption of self-preservation lead to an analytical solution in the form of a similarity function that has an additional dependence on the ratio of gravitational settling and turbulent diffusion velocities. Similar arguments are used to predict patterns of deposition onto the surface downstream of the source. Theoretical predictions are tested using a suite of large-eddy-simulation numerical experiments, with good agreement. The combined analysis of theoretical and numerical results reveals interesting features in the patterns of downstream deposition, such as non-monotonic trends in isolation distance with particle settling velocity and surprisingly large isolation distances for practically relevant parameter ranges. Possible effects of turbulence on effective settling velocity are highlighted.

Key words: atmospheric flows, particle/fluid flows, turbulent boundary layers

---

1. Introduction

The problem of dispersion of small particles emitted from an area source into a turbulent boundary layer flow is of considerable relevance in a number of settings. For example, the determination of patterns of wind dispersal and ground deposition of pollen grains is a key step in the quantification of gene flow for wind-pollinated species. Predicting pollen dispersion plays an important role in studies of genetic diversity in natural populations (Honnay *et al.* 2005; Sork & Smouse 2006; O'Connell, Mosseler & Rajora 2007) and ecological risks associated with the commercial release of genetically modified crops (Messeguer 2003). As a specific example, it is important to predict accurately at what distance to place fields with unmodified crops downwind of fields with modified crops, in order to prevent cross-fertilization. Patterns of pollen dispersion have been studied using field experiments (Raynor, Ogden & Hayes 1970; Raynor, Hayes & Ogden 1972*a*; Raynor, Ogden & Hayes 1972*b*; McCartney &

† Email address for correspondence: chamecki@meteo.psu.edu

Lacey 1991; Jarosz *et al.* 2003; Klein *et al.* 2003; van Hout *et al.* 2008) and numerical simulations (Jarosz, Loubet & Huber 2004; Dupont, Brunet & Jarosz 2006; Arritt *et al.* 2007; Chamecki, Meneveau & Parlange 2009). However, the lack of a sound theoretical framework to interpret different data sets has prevented generalizations about pollen dispersion.

In this paper we study dispersion of small particles emitted from an area source of finite size at the bottom of a fully developed turbulent boundary layer as a model for the dispersion of pollen grains in the neutrally stratified atmosphere. Most of the theoretical work on particle dispersion in boundary layers and channel flows has been based on experiments (Snyder & Lumley 1971; Rashidi, Hetsroni & Banerjee 1990; Kaftori, Hetsroni & Banerjee 1995) and detailed direct numerical simulations (McLaughlin 1989; Pedinotti, Mariotti & Banerjee 1992; Rouson & Eaton 2001; Marchioli & Soldati 2002) and aimed at fundamental mechanisms of particle–turbulence interactions. In particular, significant progress has been made in understanding preferential concentration (Squires & Eaton 1991; Rouson & Eaton 2001; Coleman & Vassilicos 2009), turbophoresis (Reeks 1983; Brooke *et al.* 1992), the role of turbulence coherent structures on particle transport and deposition (Brooke *et al.* 1992; Pedinotti *et al.* 1992; Marchioli & Soldati 2002), and the modification of turbulence by particles (Kiger & Lasheras 1997; Ahmed & Elghobashi 2000; Hartel, Meiburg & Necker 2000; Necker *et al.* 2005).

On the other hand, theoretical work on dispersion of particles in the atmospheric boundary layer follows the pioneering work of Prandtl (1952) and is restricted to predicting equilibrium profiles over horizontally homogeneous sources (Chamberlain 1967; Kind 1992; Chamecki *et al.* 2007) or dispersion from point and line sources (Rounds 1955; Godson 1957; Bouvet & Wilson 2006). Less is known about the problem of a finite-size area source in which horizontal heterogeneity and local advection play a critical role.

Turbulent transport from area sources in the atmospheric boundary layer has its roots in the study of water vapour transport and associated evaporation rates from lakes and other wet surfaces (Brutsaert 1982). The problem was first formulated by Sutton (1934), whose motivation was the prediction of evaporation rates from large reservoirs based on measurements made with evaporimeters (i.e. very small area sources). This problem is usually referred to as 'Sutton's problem' in the literature (Brutsaert 1982). Sutton obtained analytical solutions for vertical water mixing ratio profiles taking into account vertical turbulent transport and mean horizontal advection. The approach was later refined by Frost (1946) and others (Calder 1949; Philip 1959; Yeh & Brutsaert 1970). The theory was later extended to the study of momentum and scalar transport induced by step changes in the boundary conditions (such as changes in roughness, temperature, etc.), where the concept of internal boundary layers (IBL) originated (for a detailed discussion see Garratt 1994).

In this work, we extend the ideas of local advection and internal boundary layers to dispersion of heavy particles emitted from a finite-size area source. We consider a two-dimensional steady-state problem and seek boundary layer solutions for the mean particle concentration field incorporating the effects of gravitational settling. In addition, an equation for the growth of the particle concentration boundary layer is obtained. Similar assumptions lead to a prediction of the functional form of the surface deposition downstream of the source. Working assumptions and theoretical results are presented in § 2. Numerical experiments using a large-eddy-simulation model (Chamecki *et al.* 2009) are presented in support of the theoretical results in § 3. The theoretical framework developed is applied to a problem of practical interest

Parameter	Symbol	Range	Unit	Reference
Density	ρ_p	$500 < \rho_p < 1500$	kg m^{-3}	Gregory (1973, table II)
Diameter	d_p	$10 < d_p < 100$	μm	Gregory (1973, figure 3)
Relaxation time	τ_p	$0.15 < \tau_p < 46$	m s^{-1}	From (2.2)
Stokes number	St	$0.002 \leqslant St \leqslant 0.65$	—	See text

TABLE 1. Typical characteristic scales for pollen grains.

(the effects of the size of the area source on particle deposition downwind) in § 4. Results are further discussed in § 5.

2. Particle concentration boundary layer: analytical solution

2.1. *Eulerian description of particle concentration field*

In this section an Eulerian approach is used to describe transport of a plume of monodisperse particles in a turbulent boundary layer. In order to obtain analytical solutions for the mean particle concentration field, a simplified approach is required. For monodisperse particles mass density and number density are proportional and can be represented by a concentration field $C(\boldsymbol{x}, t)$. Particles are assumed to occupy a very small volume fraction, having a negligible effect on the flow field (Elghobashi 1994). In this work, it is further assumed that the particle phase moves with the turbulent velocity $\boldsymbol{u}(\boldsymbol{x}, t)$ except for a 'mean drift' velocity $-w_s \boldsymbol{e}_3$, due to gravitational settling in the vertical direction (unit vector $\boldsymbol{e}_3$). Under these assumptions, the governing equation for the concentration field is given by

$$\frac{\partial C}{\partial t} + (\boldsymbol{u} - w_s \boldsymbol{e}_3) \cdot \boldsymbol{\nabla} C = 0, \tag{2.1}$$

where diffusion due to Brownian motion has been neglected. The one-way coupling assumption is justified since while pollen concentrations close to the source field may be very high (as high as several thousand grains per cubic metre Martin, Chamecki & Brush 2010), the small volume of pollen particles leads to very small volume fractions (typically $<10^{-9}$). The mass loading is also very small, typically $<10^{-6}$. Hence the effects of particles on the flow are clearly negligible. Density and size of pollen grains (represented by ρ_p and d_p, respectively) vary from species to species and a typical range of values is presented in table 1. Assuming a typical value of the Kolmogorov length scale in the atmospheric boundary layer to be $\eta \approx 1$ mm (Kaimal & Finnigan 1994), both $\rho_p / \rho_{air} \gg 1$ and $d_p / \eta \ll 1$ hold for the entire range of pollen grains. The range of values of the particle relaxation time scale, τ_p, defined as

$$\tau_p = \frac{\rho_p d_p^2}{18 \mu}, \tag{2.2}$$

is also shown in table 1. Considering a typical value of the Kolmogorov time scale $\tau_\eta \approx 0.07$ s in the atmospheric surface layer leads to a range $0.002 \leqslant St \leqslant 0.65$. Therefore, except for the (few) largest pollen grains, the particle inertia is negligible (an important exception being corn pollen with $d_p \approx 100$ μm and $\rho_p \approx 1230$ kg m^{-3} (Aylor 2002) yielding $St \approx 0.54$).

The Eulerian transport equation with a drift velocity term has often been used before in a wide range of problems including sediment transport (Zedler & Street 2001;

Chou & Fringer 2008), gravity currents (Necker *et al.* 2002), pollen dispersion (Dupont *et al.* 2006; Chamecki *et al.* 2009), and snow drift (Lehning *et al.* 2008). The use of a drift velocity can be justified based on typical scales of the problem. Assuming the ratio between particle and fluid densities to be large ($\rho_p / \rho_f \gg 1$) and the particles to be much smaller than the Kolmogorov scale, the velocity of the particle phase $\boldsymbol{v}_p$ can be approximated by (Maxey & Riley 1983; Shotorban & Balachandar 2007)

$$\frac{\mathrm{d}\boldsymbol{v}_p}{\mathrm{d}t} = \boldsymbol{g} + \frac{\boldsymbol{u} - \boldsymbol{v}_p}{\tau_p}, \tag{2.3}$$

where $\boldsymbol{g}$ is the gravitational acceleration. Assuming the particle Stokes number $St = \tau_p / \tau_\eta$ to be small, the particle response to surrounding fluid is fast and the particle velocity can be approximated by its quasi-equilibrium relaxation value (Shotorban & Balachandar 2007)

$$\boldsymbol{v}_p = \boldsymbol{u} + \tau_p \boldsymbol{g} - \tau_p \frac{\mathrm{D}\boldsymbol{u}}{\mathrm{D}t}. \tag{2.4}$$

The second term is expressed as $\tau_p \boldsymbol{g} = -w_s \boldsymbol{e}_3$, where w_s is the particle settling velocity and represents the 'mean drift' due to gravitational settling. As shown in Shotorban & Balachandar (2007), the third term on the right-hand side of (2.4) can be used to model realistic trends such as preferential concentrations and possible effects of turbulence–particle interactions in modifying the mean settling velocity of particles. In this work, the emphasis will be on ensemble-averaged concentration fields in the context of analytically tractable solutions. To treat flows in which the settling velocity is enhanced by turbulence (Maxey 1987; Wang & Maxey 1993; Aliseda *et al.* 2002), we will proceed by assuming that w_s is then chosen to be equal to such an effective settling velocity, instead of including the third term proportional to fluid acceleration. Such an approach will enable us to obtain analytical solutions (see below). Some numerical simulations including the acceleration term are presented in § 3.3 in order to quantify possible effects of this term on mean concentrations and deposition rates.

2.2. *Mean field and problem description*

In this section we consider a fully developed turbulent boundary layer over a rough surface characterized by a roughness length z_0. Hereafter x, y and z are streamwise, spanwise and vertical directions respectively. We study a simplified problem in which the source emitting particles is the semi-infinite plane ($x \geqslant 0, -\infty < y < \infty, z = z_{0,c}$). The distance, $z_{0,c}$, between the source plane and the ground can be interpreted as a particle concentration roughness length. The source is characterized by a constant concentration $\overline{C}_0$ and a plume of particles starts developing from $x = 0$. The turbulent boundary layer height is assumed to be much larger than the height of the particle plume $\delta_c(x)$. We further assume the turbulent fluxes in the streamwise direction to be negligible in comparison to the mean advective fluxes (i.e. the boundary layer approximation). Figure 1 shows a sketch of the geometry considered.

Under these conditions, the mean particle concentration is a steady two-dimensional field $\overline{C}(x, z)$ and (2.1) yields

$$\bar{u}(z)\frac{\partial \overline{C}}{\partial x} - w_s \frac{\partial \overline{C}}{\partial z} = \frac{\partial}{\partial z}\left(K_c(z)\frac{\partial \overline{C}}{\partial z}\right), \tag{2.5}$$
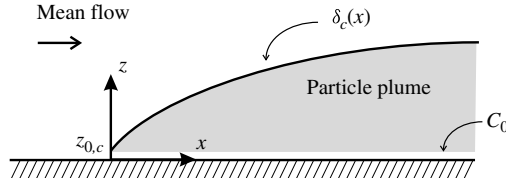
FIGURE 1. Sketch of the problem showing the coordinate system and pollen boundary layer height $\delta_c(x)$ and particle roughness height $z_{0,c}$.

where $K_c(z)$ is an eddy diffusivity used to model the vertical turbulent particle flux. The set of boundary conditions for the proposed problem is given by

$$\overline{C}(x = 0, z) = 0, \tag{2.6}$$

$$\overline{C}(x, z \to \infty) = 0, \tag{2.7}$$

$$\overline{C}(x, z = z_{0,c}) = \overline{C}_0, \tag{2.8}$$

and the solution is limited to the half-space $x > 0$. Except for the settling velocity of the particles (i.e. the second term on the left-hand side of (2.5)), this problem is the same as the one first studied by Sutton (1934) in the context of evaporation. The analysis and assumption of a constant $\overline{C}_0$ should be understood as a 'quasi-steady' approach: over any given time interval over which the wind is reasonably constant (e.g. 10 min time intervals), the fraction of pollen being released is assumed to be much smaller than the reservoir content.

In order to close the set of equations, the mean wind and eddy-diffusivity profiles must be specified. As is often done in analytical solutions for problems including local advection, we adopt power-law profiles to simplify the mathematical formulation (see Brutsaert 1982, p. 160)

$$\overline{u}(z) = u_* C_p \left(\frac{z}{z_o} \right)^m, \quad K_c(z) = \frac{\kappa u_* z}{Sc}, \tag{2.9}$$

where u_* is the friction velocity, κ is the von Kármán constant, and Sc is the turbulent Schmidt number for particle concentration. For neutral temperature stratification typical values adopted for the constants specifying the mean wind profile are $C_p \approx 6$ and $m = 1/7$ (Brutsaert 1982).

Using the power-law profiles, the governing equation (2.5) can be written as

$$z \frac{\partial^2 \overline{C}}{\partial z^2} + (1 + \gamma) \frac{\partial \overline{C}}{\partial z} - \frac{Sc C_p}{\kappa} \left(\frac{z}{z_o} \right)^m \frac{\partial \overline{C}}{\partial x} = 0, \tag{2.10}$$

where

$$\gamma = \frac{Sc}{\kappa} \frac{w_s}{u_*} \tag{2.11}$$

is a dimensionless parameter usually referred to as the 'Rouse number' in studies of sediment transport in rivers (Rouse 1937), representing the relative importance of turbulent dispersion and gravitational settling (e.g. see Chamecki *et al.* 2007).

2.3. *Similarity solution*

Following the standard approach in boundary layer problems, local scales are defined and self-preservation of the dimensionless concentration profile is assumed. If the

correct scales are chosen for the similarity variables, the approach allows one to transform the partial differential equation (2.10) to an ordinary differential equation. The validity of the assumptions made will be tested through comparison with numerical simulation data presented in § 3.

The concentration profile at any streamwise location is scaled by its maximum value $\overline{C}_{max}(x)$. In addition, a particle concentration boundary layer height $\delta_c(x)$ can be defined as the height where the concentration has dropped to a fixed fraction of its maximum value. Therefore, the assumption of self-preservation yields

$$\frac{\overline{C}(x,z)}{\overline{C}_{max}(x)} = g(\eta), \tag{2.12}$$

where $\eta = z/\delta_c(x)$ is the similarity variable and $g(\eta)$ is a similarity function, which depends, in addition to η, on the parameter γ. For the specific problem described above, where the concentration is imposed and maximum at the surface $z = z_{0,c}$, we have $\overline{C}_{max}(x) = \overline{C}_0$, which is constant.

Expressing the independent variables x and z in terms of the similarity variable η, the resulting equation is given by

$$\frac{\mathrm{d}^2 g}{\mathrm{d}\eta^2} + (1+\gamma)\frac{1}{\eta}\frac{\mathrm{d}g}{\mathrm{d}\eta} + \frac{ScC_p}{\kappa z_0^m}\left(\delta_c^m\frac{\mathrm{d}\delta_c}{\mathrm{d}x}\right)\eta^m\frac{\mathrm{d}g}{\mathrm{d}\eta} = 0. \tag{2.13}$$

For a self-similarity solution to exist, no x-dependence can remain in the equation above. This is only possible if the product $\delta_c^m(\mathrm{d}\delta_c/\mathrm{d}x)$ is a constant. Note that this constant may depend on the parameter γ. For convenience, we define the constant as

$$C_1(\gamma) = \frac{ScC_p}{\kappa z_0^m}\left(\delta_c^m\frac{\mathrm{d}\delta_c}{\mathrm{d}x}\right), \tag{2.14}$$

and the final form of the ordinary differential equation (ODE) becomes

$$g'' + \left[\frac{(1+\gamma)}{\eta} + C_1(\gamma)\eta^m\right]g' = 0, \tag{2.15}$$

where primes indicate derivatives with respect to η.

When expressing the boundary conditions using the similarity variable, notice that the first two conditions (2.6) and (2.7) collapse into

$$g(\eta \to \infty) = 0, \tag{2.16}$$

and the third boundary condition (2.8) becomes

$$g(\eta = \eta_0) = 1 \tag{2.17}$$

where $\eta_0 = z_{0,c}/\delta_c(x)$. If $z_{0,c}$ is fixed independent of x, then η_0 will depend on x and no similarity solution exists. We assume η_0 to be a constant in order to proceed (but since $\delta_c(x)$ depends on γ, we allow η_0 to depend on γ as well). The consequences of allowing $z_{0,c}$ to grow in the same manner as $\delta_c(x)$ are not expected to be highly significant and the appropriateness of this simplification will be evaluated later by comparisons with numerical simulations where this assumption is not needed.

Integrating twice (first an indefinite and then a definite integral between η and ∞), the solution to the ODE given by (2.15) is

$$g(\infty) - g(\eta) = C_I \int_\eta^\infty \zeta^{-(\gamma+1)}\exp\left[-\frac{C_1(\gamma)\zeta^{m+1}}{m+1}\right]\mathrm{d}\zeta, \tag{2.18}$$

where C_I is a constant from the first integration and ζ is an integration variable. Using the boundary condition (2.16) and the change of variables

$$t = \frac{C_1(\gamma)}{m+1}\zeta^{m+1},$$ (2.19)

the solution can be written as

$$g(\eta) = -C_I \frac{1}{m+1}\left(\frac{C_1(\gamma)}{m+1}\right)^{\gamma/(m+1)}$$

$$\times \int_{(C_1(\gamma)/(m+1))\eta^{m+1}}^{\infty} t^{-[1+\gamma/(m+1)]}\exp[-t]\,\mathrm{d}t,$$ (2.20)

or in terms of the upper incomplete gamma function $\Gamma(a,x)$

$$g(\eta) = -C_I \frac{1}{m+1}\left(\frac{C_1(\gamma)}{m+1}\right)^{\gamma/(m+1)}\Gamma\left(-\frac{\gamma}{m+1},\frac{C_1(\gamma)}{m+1}\eta^{m+1}\right),$$ (2.21)

where the upper incomplete gamma function is defined as $\Gamma(a,x) = \int_x^{\infty} t^{a-1}\mathrm{e}^{-t}\,\mathrm{d}t$. Finally, imposing the boundary condition (2.17) yields

$$g(\eta) = \frac{\Gamma\left(-\dfrac{\gamma}{m+1},\dfrac{C_1(\gamma)}{m+1}\eta^{m+1}\right)}{\Gamma\left(-\dfrac{\gamma}{m+1},\dfrac{C_1(\gamma)}{m+1}\eta_0^{m+1}\right)},$$ (2.22)

which completely specifies the particle concentration profiles if the function $C_1(\gamma)$ is known. Because $\gamma > 0$ and $m > 0$, the first argument in the incomplete gamma function above (i.e. parameter a) is always negative and most approximations based on convergent or asymptotic series fail. For numerical evaluation of the incomplete Gamma function, we use instead the algorithm implemented in the Fortran library FMLIB (Smith 2001) which works remarkably well when compared to direct numerical integration according to the fundamental definition of the function.

2.4. *Growth of the particle concentration boundary layer*

The condition for the existence of a similarity solution (2.14) can be used to derive an expression for the growth of the particle concentration boundary layer δ_c. The condition can be written as

$$\delta_c^m \frac{\mathrm{d}\delta_c}{\mathrm{d}x} = C_1(\gamma)\frac{\kappa z_0^m}{ScC_p}.$$ (2.23)

Assuming $\delta_c(x=0) = 0$, the expression above can be integrated to yield

$$\delta_c(x) = \left[C_1(\gamma)\frac{\kappa z_0^m}{ScC_p}(m+1)x\right]^{1/(m+1)},$$ (2.24)

where the function $C_1(\gamma)$ is the only unknown. Strictly speaking, the initial condition for the integration above should be $\delta_c(x=0) = z_{0,c}$, but the expressions become a bit more complicated and it makes no appreciable difference in practice.

One more constraint is needed to determine $C_1(\gamma)$. An independent approximate expression for $\delta_c(x)$ can be obtained by analogy with the ideas used to predict the growth of internal boundary layers for momentum and passive scalars due to changes

in surface conditions (e.g. see Brutsaert 1982; Garratt 1994). The usual assumption is that the rate of growth of the internal boundary layer ($d\delta/dt$) is proportional to the root-mean-square of vertical velocity fluctuations σ_w:

$$\frac{d\delta}{dt} = C_w \sigma_w, \qquad (2.25)$$

where $C_w = O(1)$ is a constant of proportionality. In addition, invoking Taylor's frozen turbulence hypothesis and assuming $\sigma_w = 1.25 u_*$ for neutral conditions (e.g. Kaimal & Finnigan 1994) one can write

$$\frac{d\delta}{dx} = \frac{C_w \sigma_w}{\bar{u}} = \frac{1.25 C_w u_*}{\bar{u}}. \qquad (2.26)$$

In the context of internal boundary layers, expression (2.26) is then integrated using $\bar{u}(z = \delta)$ in the denominator of the right-hand side. Using results from large-eddy simulation (LES), $1.25 C_w \approx 0.85$ was found to be a good approximation to describe the growth of internal momentum boundary layers over an abrupt change in surface roughness (Bou-Zeid, Meneveau & Parlange 2004).

In the present case, a similar approach can be used to predict $\delta_c(x)$. However, the growth rate of the particle plume is now reduced by the gravitational settling, and if we assume a linear combination of both rates, one may write

$$\frac{d\delta_c}{dt} = C_w \sigma_w - w_s. \qquad (2.27)$$

Such a linear combination of growth rates is used here as the simplest possible modelling choice. Deviations from linear superposition could be expected especially when the growth processes are both fast.

Using Taylor's hypothesis and the power-law (2.9) to specify $\bar{u}(z = \delta_c)$, (2.27) can be written as

$$\delta_c^m \frac{d\delta_c}{dx} = \left[\frac{1.25 C_w Sc}{\kappa} - \gamma \right] \frac{\kappa z_0^m}{Sc C_p}. \qquad (2.28)$$

Comparison between (2.23) and (2.28) yields

$$C_1(\gamma) = \left(\frac{1.25 C_w Sc}{\kappa} - \gamma \right). \qquad (2.29)$$

Therefore, the final similarity solution is given by equations (2.22), (2.24), and (2.29). Figure 2(a) shows a series of predicted concentration profiles for various γ values, while figure 2(b) shows the corresponding growth of the concentration boundary layer height. The following parameters have been used in these visualizations: $1.25 C_w = 0.85$, $Sc = 0.5$, $\kappa = 0.4$, $m = 1/7$, $C_p = 6$, $z_0 = 0.01$ m, $z_{0,c} = 0.01$ m, $L = 1000$ m (η_0 was calculated using $\eta_0 = z_{0,c}/\delta_c(x = L/2)$, as discussed in § 3.2).

The thin solid lines in figure 2(a) show the solution with $\gamma = 0.25$ but using an increase/decrease of $z_{0,c}$ by 25 % (this translates into an increase/decrease of 25 % in η_0). There is a shift of the inner part of the profile depending on the value of η_0. As can be expected, in the near-surface region close to the emission height, the concentration will depend significantly on distance to the emission height. Therefore, for applications in which $z_{0,c}$ is a constant physical height (i.e. when η_0 varies as a function of x), the assumption made in the similarity solution that η_0 is constant does not, strictly speaking, hold. Still, the aim is to employ the similarity solution in the sense of a 'quasi-steady' solution, using a representative value of η_0. The accuracy
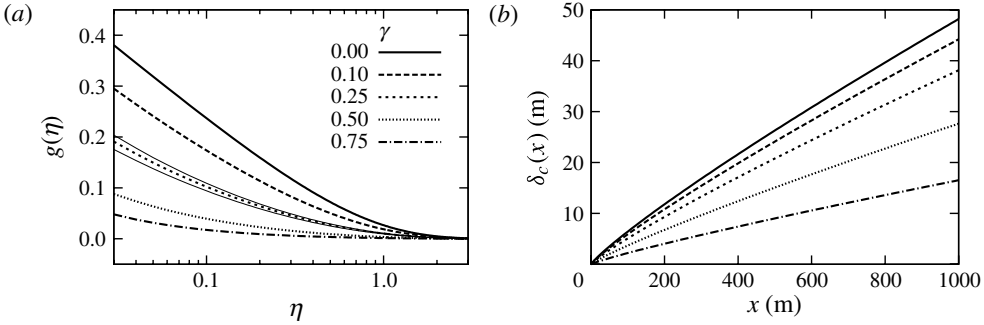
FIGURE 2. Theoretical profiles (*a*) $g(\eta)$ and (*b*) $\delta_c(x)$ for various values of γ (other parameters listed in the text). Thin solid lines in (*a*) represent a variation of $\pm 25\,\%$ in $z_{0,c}$ for $\gamma = 0.25$.

of the consequences of these assumptions will be tested in detail using large-eddy simulations, in § 3. Among other things, it will be shown that concentration profiles display excellent collapse when plotted using the proposed similarity variables.

2.5. *Scaling deposition downstream from a finite source*

In most practical applications, a quantity of significant interest is the surface deposition downstream of the area source. Let us consider a source field of length L in the streamwise direction instead of the semi-infinite source (the results presented above are still valid above the source field). If we define a new coordinate system in which $\xi \equiv x - L$ (i.e. the origin is now at the trailing edge of the field), the point of interest is the decay of $\overline{C}_{max}(\xi)$ or the deposition flux onto the surface $\Phi(\xi)$ with ξ for different values of γ.

Under the same assumptions made in the previous sections, the problem downstream of the source is also governed by equation (2.10). Furthermore, due to the parabolic nature of the boundary layer equation, the concentration field downstream of the source can be solved as an initial value problem, with initial condition specified by the concentration profile at the trailing edge $\overline{C}(x = L, z) = \overline{C}(\xi = 0, z)$. The same similarity variables can be introduced, except that now $\overline{C}_{max}(\xi)$ is not a constant. Taking the ξ-dependence of the concentration scale into account and using $f(\eta) = \overline{C}(\xi, z)/\overline{C}_{max}(\xi)$ to indicate a different similarity solution, the equation becomes

$$\frac{\mathrm{d}^2 f}{\mathrm{d}\eta^2} + (1 + \gamma)\frac{1}{\eta}\frac{\mathrm{d}f}{\mathrm{d}\eta} + \frac{ScC_p}{\kappa z_o^m}\left(\delta_c^m \frac{\mathrm{d}\delta_c}{\mathrm{d}\xi}\right)\eta^m \frac{\mathrm{d}f}{\mathrm{d}\eta}$$
$$- \frac{ScC_p}{\kappa z_o^m}\left(\frac{\delta_c^{m+1}}{\overline{C}_{max}}\frac{\mathrm{d}\overline{C}_{max}}{\mathrm{d}\xi}\right)\eta^{m-1}f = 0. \tag{2.30}$$

Since both δ_c and $\overline{C}_{max}$ depend on ξ, constraint (2.14) still has to be satisfied. There is one additional requirement for the existence of a similarity solution, namely that

$$C_3(\gamma) = -\frac{ScC_p}{\kappa z_o^m}\left(\frac{\delta_c^{m+1}}{\overline{C}_{max}}\frac{\mathrm{d}\overline{C}_{max}}{\mathrm{d}\xi}\right) \tag{2.31}$$

is independent of downstream distance. The final ODE contains three terms, two of which are similar to (2.15), and is given by

$$f'' + \left[\frac{(1+\gamma)}{\eta} + C_2(\gamma)\eta^m \right] f' + C_3(\gamma)\eta^{m-1} f = 0, \tag{2.32}$$

where $C_2(\gamma)$ is used instead of $C_1(\gamma)$ to indicate that the function may actually be different from the one obtained in the previous section.

Equation (2.24) should still be valid if a non-zero initial boundary layer height $\delta_c(\xi = 0) = \delta_L$ is imposed:

$$\delta_c(\xi) = \left[\delta_L^{m+1} + C_2(\gamma)\frac{\kappa z_o^m}{ScC_p}(m+1)\xi \right]^{1/(m+1)}. \tag{2.33}$$

Replacing this expression for $\delta_c(\xi)$ into (2.31) and solving for $\overline{C}_{max}(\xi)$ yields

$$\overline{C}_{max}(\xi) = \overline{C}_{ini}(\gamma) \left[1 + C_2(\gamma)\frac{\kappa(m+1)}{ScC_p}\left(\frac{z_o}{\delta_L}\right)^m \frac{\xi}{\delta_L} \right]^{-C_3(\gamma)/(m+1)C_2(\gamma)}, \tag{2.34}$$

where the initial condition $\overline{C}_{max}(\xi = 0) = \overline{C}_{ini}(\gamma)$ was used. Equation (2.34) can be written as

$$\overline{C}_{max}(\xi) = \overline{C}_{ini}(\gamma) \left[1 + \frac{1}{b(\gamma)}\frac{\xi}{\delta_L} \right]^{-\beta(\gamma)}, \tag{2.35}$$

where the following definitions were used:

$$b(\gamma) = \left[C_2(\gamma)\frac{\kappa(m+1)}{ScC_p}\left(\frac{z_o}{\delta_L}\right)^m \right]^{-1}, \tag{2.36}$$

$$\beta(\gamma) = \frac{C_3(\gamma)}{(m+1)C_2(\gamma)}. \tag{2.37}$$

Finally, the deposition on the bottom surface is the total vertical flux at the surface. From (2.5) we can write the total deposition flux as

$$\Phi(\xi) = \left[w_s\overline{C} + K_c\frac{\partial\overline{C}}{\partial z} \right]_{z=z_{0,c}}, \tag{2.38}$$

which can be expressed in similarity variables as

$$\frac{\Phi(\xi)}{\overline{C}_{max}(\xi)u_*} = \frac{w_s}{u_*}\left[f + \frac{\eta}{\gamma}\frac{df}{d\eta} \right]_{\eta=\eta_0}. \tag{2.39}$$

Clearly the right-hand side of (2.39) does not depend on ξ (i.e. it depends only on γ), and we can write

$$\frac{\Phi(\xi)}{\overline{C}_{max}(\xi)} = F(\gamma), \tag{2.40}$$

so that

$$\Phi(\xi) = a(\gamma) \left[1 + \frac{1}{b(\gamma)}\frac{\xi}{\delta_L} \right]^{-\beta(\gamma)}, \tag{2.41}$$

where $a(\gamma) = F(\gamma)\overline{C}_{ini}(\gamma)$. Note that according to (2.41), the dependence of the deposition flux on the field size L is given only through δ_L.

The expression for the deposition flux given by (2.41) can be further constrained based on the global particle mass balance. The horizontal particle flux across the vertical plane at the trailing edge of the source field is given by

$$F_T = \int_{z_{0,c}}^{\infty} \overline{C}(x = L, z)\overline{u}(z)\,\mathrm{d}z, \tag{2.42}$$

where the turbulent flux in the streamwise direction has been neglected as before. The expression above can be expressed in similarity variables as follows:

$$F_T = \frac{u_* C_p \overline{C}_0 \delta_L}{\eta_0^m} \int_{\eta_0}^{\infty} g(\eta)\eta^m\,\mathrm{d}\eta. \tag{2.43}$$

This expression can be integrated to yield

$$\frac{F_T}{u_*\overline{C}_0} = \frac{C_p\delta_L}{\eta_0^m}\left[\frac{1}{C_1(\gamma)}\frac{\Gamma\left(1 - \dfrac{\gamma}{m+1}, \dfrac{C_1(\gamma)}{m+1}\eta_0^{m+1}\right)}{\Gamma\left(-\dfrac{\gamma}{m+1}, \dfrac{C_1(\gamma)}{m+1}\eta_0^{m+1}\right)} - \frac{\eta_0^{m+1}}{m+1}\right]. \tag{2.44}$$

Conservation of the total particle mass requires the total deposition to be equal to F_T, i.e.

$$F_T = \int_0^{\infty} \Phi(\xi)\,\mathrm{d}\xi = \frac{a(\gamma)b(\gamma)\delta_L}{\beta(\gamma) - 1}, \tag{2.45}$$

where the assumption $\beta > 1$ was made (if this condition is not satisfied, the integral above is unbounded and the solution is unphysical). The validity of the scaling (2.41) and expression (2.44) will be investigated using numerical simulations in § 4.

3. Particle concentration boundary layer: large-eddy simulations

The focus of the numerical experiments is on pollen dispersion from fields of finite length. In order to provide meaningful comparisons with the theoretical results developed in the previous section, the source field emitting pollen is a stripe of length L and infinite width in the lateral direction. The source field is surrounded by an infinite grass field, as depicted in figure 3. The mean wind speed is assumed to be steady and perpendicular to the field (so that $\overline{v} = 0$). Other than the finite length of the field and the change in the canopy characteristics (i.e. surface roughness) between grass and source field, the physical problem is equal to the one studied in the previous section.

3.1. *Code description and numerical setup*

A suite of numerical experiments using large-eddy simulation is used to compare with the results presented in the previous section. The numerical model solves the three-dimensional filtered momentum equations in rotational form and the filtered conservation equation for pollen concentration given by

$$\frac{\partial \widetilde{C}}{\partial t} + \nabla \cdot (\widetilde{\boldsymbol{v}}_p \widetilde{C}) = -\nabla \cdot \boldsymbol{\pi}^C, \tag{3.1}$$
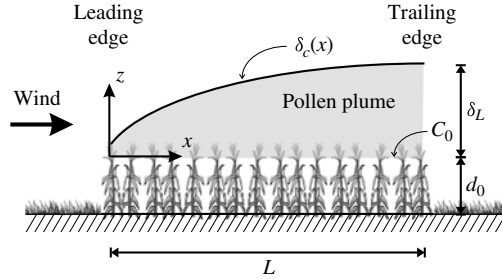
FIGURE 3. Sketch of the problem showing the pollen boundary layer height $\delta_c(x)$. The origin is shifted vertically to the displacement height $d_0 = 0.75h$.

where a tilde indicates a filtered field, $\widetilde{\boldsymbol{v}}_p = (\widetilde{\boldsymbol{u}} - w_s \boldsymbol{e}_3)$ is the resolved velocity for the particle phase, and $\boldsymbol{\pi}^C$ is the subgrid scale (SGS) pollen flux. The SGS flux is parametrized using a flux-gradient model (see Chamecki et al. 2009, for a detailed description of the model).

The momentum equations are discretized using a pseudo-spectral approach in the horizontal direction and a second-order centred finite-difference scheme in the vertical. The conservation equation for pollen concentration is discretized using a finite-volume approach in which the advective term is calculated using the bounded SMART algorithm (Gaskell & Lau 1988). The interpolations required to couple the two distinct discretization approaches are performed using the conservative interpolation scheme proposed by Chamecki, Meneveau & Parlange (2008). The velocity field is periodic in the horizontal directions. For the pollen concentration, a zero concentration inflow condition is imposed, and periodic conditions are imposed in the spanwise directions. At the outflow, a zero streamwise concentration gradient (outflow boundary condition) is imposed. Bottom boundary conditions for the momentum and pollen concentration equations are prescribed using wall layer models following the approach described in Chamecki et al. (2009) and further discussed below. The subgrid scale momentum fluxes are modelled using the dynamic Smagorinsky model (Germano et al. 1991), following the Lagrangian scale-dependent implementation (Meneveau, Lund & Cabot 1996; Bou-Zeid, Meneveau & Parlange 2005). Subgrid scale pollen fluxes are modelled using a flux-gradient model with the SGS diffusivity obtained from the Lagrangian dynamics SGS viscosity and a constant SGS Schmidt number. The numerical model is described in detail in Chamecki et al. (2009), where it is also validated against experimental data of point source releases and dispersion of pollen released from a natural ragweed field.

A total of 14 simulations were performed to study the effects of $\gamma = Sc w_s/(\kappa u_*)$ and the size of the source field L on pollen dispersion. The general details of the simulation setup and numerical grid are presented in table 2. In all simulations the flow is in equilibrium with a grass surface (characterized by a roughness length scale $z_0 = 0.01$ m in the lower boundary condition for momentum) when it reaches a canopy patch with uniform height $h = 1$ m. Note that the vertical height of the plants is not resolved on the simulation ($dz = 3$ m) and is parametrized through the lower momentum boundary conditions as well (using a displacement height $d_0 = 0.75h$ and roughness $z_0 = h/8$ for the canopy). The canopy patch extends infinitely in the spanwise direction and has a length L varying between $L = 60h$ and $L = 480h$ in the streamwise direction. The pollen emission is prescribed by imposing $\overline{C} = \overline{C}_0$ above the source field (i.e. at $z_{0,c} = d_0 + z_0$). The numerical bottom boundary condition

Parameter	Symbol	Value	Unit
Grid points	$N_x \times N_y \times N_z$	$200 \times 100 \times 100$	—
Domain size	$L_x \times L_y \times H$	$3000 \times 1500 \times 300$	m
Grid spacing	$d_x \times d_y \times d_z$	$15 \times 15 \times 3$	m
Total time	T	3600	s
Time step	dt	0.1	s
Friction velocity	u_*	0.4	m s^{-1}
SGS Schmidt number	Sc_{sgs}	0.4	—
Pollen concentration at the source	$\overline{C}_0$	500	grains m^{-3}

TABLE 2. Parameters and setup for simulations.

is the specification of the total vertical pollen flux between the bottom surface and the first vertical grid level $z = z_1$. Therefore, the imposed constant concentration is not directly used as a boundary condition in the numerical model. Instead, it is used to obtained the required flux. This is done by substituting the imposed constant concentration into the wall-function for settling particles proposed by Chamecki *et al.* (2007), yielding

$$\Phi_{model}^{src}(x,y) = -w_s \frac{\widetilde{C}(x,y,z_1) - \overline{C}_0 \left(\dfrac{z_1 - d_0}{z_{0,c} - d_0} \right)^{-\gamma}}{1 - \left(\dfrac{z_1 - d_0}{z_{0,c} - d_0} \right)^{-\gamma}}, \tag{3.2}$$

where $\widetilde{C}(x,y,z_1)$ is the resolved concentration at the first vertical grid level. The grass field (both upwind and downwind from the source field) is assumed to be a fully absorbent surface, represented by imposing $\overline{C} = 0$ at $z_{0,c} = z_0$. Substituting these values into the wall-function and noting that $d_0 = 0$ above the grass yields

$$\Phi_{model}^{grass}(x,y) = -w_s \widetilde{C}(x,y,z_1) \left(\frac{z_1^{\gamma}}{z_1^{\gamma} - z_{0,c}^{\gamma}} \right). \tag{3.3}$$

The boundary condition above the source field given by (3.2) represents the net result of the pollen release flux and deposition flux onto the source field, while the boundary condition for the grass field given by (3.3) is the deposition onto the grass. In both equations, the fluxes represent the combined effects of deposition by gravitational settling and vertical transport by turbulence (for a detailed description, see Chamecki *et al.* 2009).

All simulations were evolved until the velocity field reached a statistically steady condition and then pollen release was started. Statistics were accumulated after the pollen plume reached a statistically steady state. The relative importance of turbulent dispersion and gravitational settling was investigated by varying the parameter γ from $\gamma = 0$ (no settling velocity) to $\gamma = 0.625$ (in the calculation of values of γ from the LES, we use the ensemble average value for the turbulent Schmidt number $Sc = 0.5$, which was estimated from a simulation using $\gamma = 0$).

Snapshots of the particle concentration field in the x–z plane are shown in figure 4 for $\gamma = 0.125$ and (*b*) $\gamma = 0.625$. In the figure, the source field is located in the range $82.5 \text{ m} \leqslant x \leqslant 562.5 \text{ m}$ and the mean flow is from left to right. Both plots correspond to the same time step (and therefore the same resolved velocity field) and
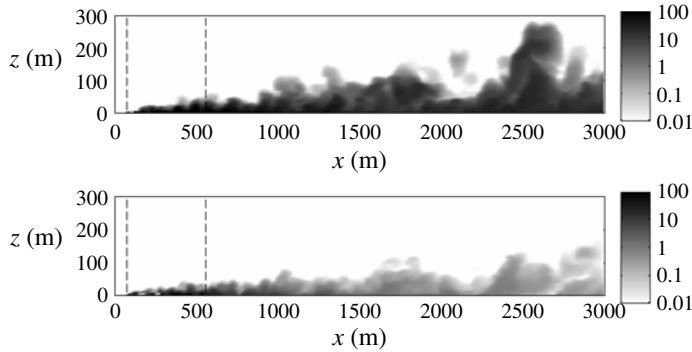
FIGURE 4. Snapshots of iso-contours of resolved pollen concentration (x–z plane) for (a) $\gamma = 0.125$ and (b) $\gamma = 0.625$. Dashed lines indicate the horizontal extent of the source field.

the differences in the details of the plumes illustrate the effects of increasing the settling velocity: the pollen concentrations are much lower and the plume height is reduced.

3.2. *Numerical results*

In this section the time-averaged particle concentration plume (i.e. hereafter overbars are interpreted as time-averaging) above the source field is investigated for the largest field size $L = 480h$. For comparison with the theoretical results, the origin is shifted vertically to the displacement height d_0 as indicated in figure 3. Nine mean concentration profiles at different distances from the leading edge of the field are shown in figure 5(a) for the case $\gamma = 0.125$, showing the increase in pollen load with distance from the edge. Note that since $\overline{C}_{max}(x)$ is constant above the source field, the normalization on the x-axis has no effect on the relative loads. The pollen boundary layer height $\delta_c(x)$ is determined from the simulation profiles as the point where $\overline{C}(\eta = \delta_c)/\overline{C}_{max} = 0.01$ (linear interpolation is used between two vertical grid points). As shown in figure 5(b), if the height is normalized by the pollen boundary layer height at each location, all curves collapse, confirming the validity of the self-preservation assumption. Therefore, we conclude that the results from the numerical simulation support the existence of a similarity solution and the validity of the condition (2.14). Figure 5(c, d) shows similar results downstream from the source field (now taking into account the ξ-dependence of $\overline{C}_{max}$), confirming the existence of a similarity solution as well, and supporting the validity of condition (2.31).

Figure 6 compares LES results to the theoretical predictions above the source field for all eight values of γ used in numerical simulations (self-preservation holds for all values tested). Concentrations obtained at the first vertical grid level (i.e. the isolated set of points on the far left of each panel in the figure) do not collapse well, but this is probably an issue of numerical resolution. The agreement between theoretical predictions given by (2.22) and (2.29) and the LES results is quite good for all ranges of γ and small values of η. To evaluate the theoretical predictions, a value of η_0 appropriate to the simulations is required. It is obtained according to $\eta_0 = z_{0,c}/\delta_c(x = L/2)$, i.e. an average value for the field using the pollen concentration boundary layer height in the middle of the field at $x = L/2$. Theoretical predictions improve with increasing γ for large values of η, being good for the entire range of η for $\gamma > 0.438$. This improvement in agreement can be explained as follows: for larger γ, the effect of gravitational settling becomes more important and the pollen boundary layer height
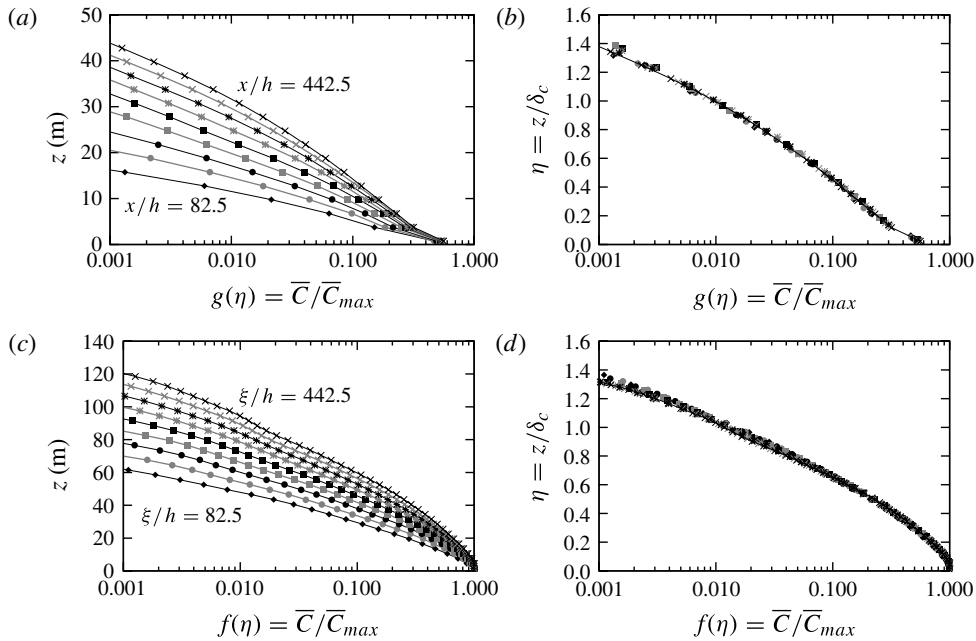
FIGURE 5. Average pollen concentration profiles above the source field normalized by local maximum concentration at different distances from the leading edge x/h (from $x/h = 82.5$ to $x/h = 442.5$ in increments of 50) for $\gamma = 0.125$. (*a*) Plotted against height above the ground and (*b*) against dimensionless height η illustrating collapse consistent with self-preservation. Panels (*c*) and (*d*) are similar for concentration profiles downstream from the source at different distances from the trailing edge ξ/h.

growth is reduced (as suggested by (2.24) and (2.29) and illustrated by numerical results in the sequence). Therefore, for larger values of γ, the entire particle plume is within the surface layer, where the eddy-diffusivity scaling of $K_c(z)$ proportional to wall distance, as well as the power-law profiles for $\bar{u}(z)$, represent a reasonable approximation.

Another interesting feature of figure 6 is the behaviour of the theoretical predictions in the lower portion of the concentration boundary layer, given by $\eta < 0.1$. Within this region, the assumption that the vertical net flux is constant leads to a logarithmic profile for $\gamma = 0$ (e.g. see Kader & Yaglom 1972), which is confirmed by the approximately straight line in figure 6(*a*). As the value of γ increases, the profile not only shifts but also becomes curved, more consistent with the power-law profiles derived for particle concentration in the constant flux region (e.g. see Chamberlain 1967; Kind 1992; Chamecki *et al.* 2007).

Next, the growth of the particle concentration boundary layer above the source field is investigated. As stated before, boundary layer heights are obtained from the numerical simulations defined as the height where $\overline{C}/\overline{C}_{max} = 0.01$, and are shown in figure 7(*a*) for a range of values of γ. The plot confirms that the boundary layer growth depends strongly on the relative importance of turbulent dispersion and gravitational settling, and that using the value $\overline{C}/\overline{C}_{max} = 0.01$ to define δ_c yields good agreement with the theory. Notice that the boundary layer height at $x = 0$ is not zero as assumed in the derivation of (2.24). This initial non-zero δ_0 is probably caused by the discontinuity in canopy properties. In order to make a comparison with the theoretical
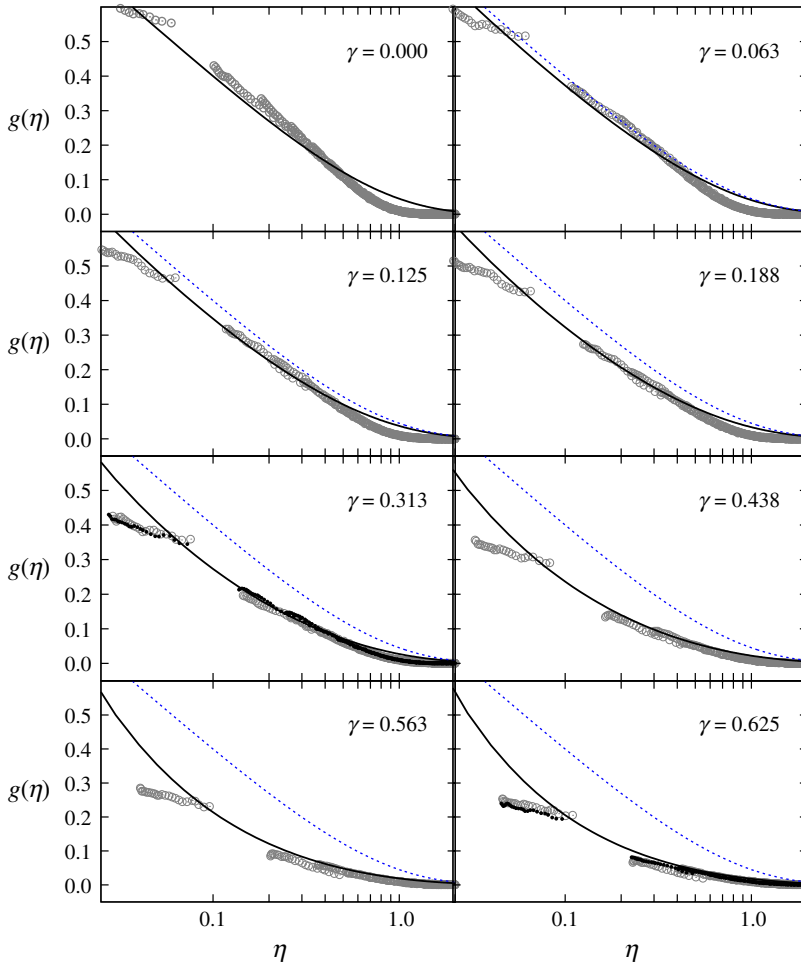
FIGURE 6. Normalized concentration profiles as a function of height above the surface. Different panels show the similarity function $g(\eta)$ for different values of γ, as indicated. Symbols represent data from the numerical simulations, solid lines are obtained from (2.22) and (2.29), and the dashed line is the solution for $\gamma = 0$ (no settling velocity) shown as reference. Small black symbols indicate simulations discussed in § 3.3.

prediction possible, a virtual origin x_0 is fitted to a single value optimizing all curves. The value obtained here is $x_0 = -64.25h$, but this value is likely to be dependent on several parameters not investigated here (such as the change in roughness between the two surfaces, the friction velocity, etc.). This is the only fitted parameter to connect the theoretical model to the LES, since all other constants are set to the values obtained from the literature and cited in the text (the roughness of the source field is used). The comparison between values calculated in the simulation and predictions made using (2.24) and (2.29) are plotted against each other in figure 7(b) (a one-to-one line representing a perfect model is shown for reference). The agreement between the theoretical boundary layer growth and the values obtained from the numerical experiments is quite good for the entire range of γ.

Next, we verify the validity of the expression (2.44) to predict the total flux of pollen across the trailing edge of the field. The theoretical result (2.44) is compared to
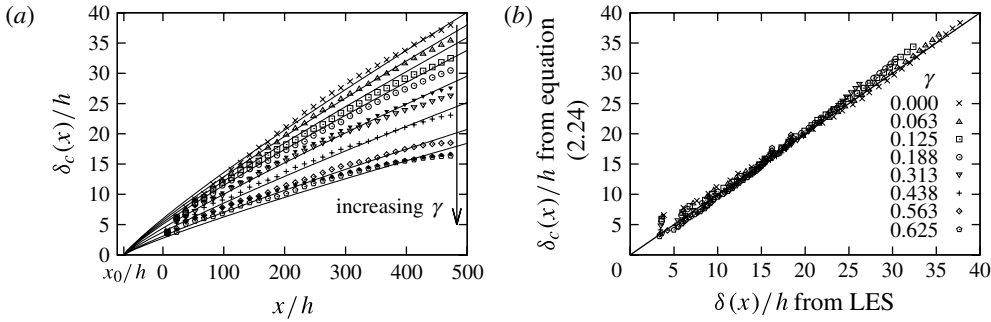
FIGURE 7. (*a*) Growth of the pollen concentration boundary layer with distance from the leading edge showing the effect of γ. Symbols are results from the numerical experiments and lines are predictions from (2.24) and (2.29) with $x_0 = -64.25h$ (as discussed in the text). (*b*) Comparison between values obtained from LES and using the analytical solution. Small black symbols indicate simulations discussed in § 3.3.
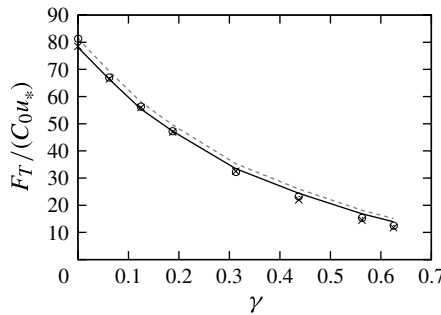

FIGURE 8. Total horizontal flux across trailing edge of the source field: numerical integration of expression (2.43) (solid line), explicit solution given by (2.44) (dashed grey line), mean advective flux from LES (circles), and flux obtained from pollen mass balance from LES (crosses).

the numerical integration of expression (2.44) and to two different estimates obtained from the LES results in figure 8. Agreement is quite good between all four methods, confirming that predictions obtained from (2.44) are correct.

3.3. *Effects of particle inertia*

In order to quantify effects of the neglected fluid acceleration term on mean particle velocity (i.e. the third term on the right-hand side of (2.4)), two extra simulations ($\gamma = 0.313$ and $\gamma = 0.625$) are performed including the resolved part of the fluid acceleration. This is done by specifying

$$\widetilde{\boldsymbol{v}}_p = \widetilde{\boldsymbol{u}} - w_s \boldsymbol{e}_3 - \tau_p \frac{\mathrm{D}\widetilde{\boldsymbol{u}}}{\mathrm{D}t} \tag{3.4}$$

in the calculation of the velocity for the particle phase used in (3.1). This is the approach proposed by Shotorban & Balachandar (2007) for the resolved velocity of the particle phase. No modifications were made to the boundary conditions given by (3.2) and (3.3) or the SGS eddy-diffusivity model for particle concentration. The numerical implementation of (3.4) is done by calculating $\mathrm{D}\widetilde{\boldsymbol{u}}/\mathrm{D}t$ explicitly in the code from the
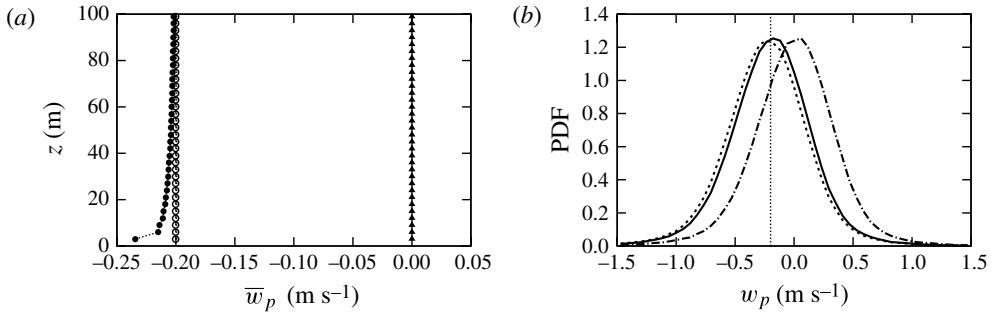
FIGURE 9. (*a*) Vertical profile of the average components of particle vertical velocity: resolved fluid velocity (triangles), settling velocity (open circles), and resolved fluid acceleration (closed circles). (*b*) Probability density function of vertical particle velocity at the first vertical grid level $z = 1.5$ m: resolved fluid velocity only (dot-dashed line), including settling velocity (solid line), and including settling velocity and resolved fluid acceleration (dashed line). The vertical dotted line indicates the prescribed settling velocity.

terms in the right-hand side of the equation (i.e. adding the SGS stress divergence and the resolved pressure gradient). The result is added together with the imposed settling velocity to the resolved fluid velocity (linear interpolations are used where needed for the fluid acceleration). This resulting velocity for the particle phase is then used as the advective speed in the SMART scheme (i.e. to determine the direction of advection and select the points for the surface flux estimation). The simulations are performed in the same fashion as described before.

In order to estimate the net effects of the additional acceleration term, first the averages of particle velocities are computed during the simulation. The resulting vertical profile for the averages of the three terms contributing to the particle vertical velocity are shown in figure 9(*a*) for the case $\gamma = 0.625$ (i.e. the one for which inertial effects are the largest). In agreement with previous studies (Maxey 1987; Wang & Maxey 1993; Aliseda *et al.* 2002), particle inertia increases the vertical settling velocity. This increase is more pronounced closer to the ground, being as large as about 17 % at the first vertical grid level and 7 % at the second. As expected, mean particle velocities in the horizontal directions (not shown) are essentially zero in this flow. To further study manifestations of this effect, the probability density function (PDF) of the particle velocity at the first vertical grid level is shown in figure 9(*b*) with and without the inclusion of the acceleration term. The inclusion of the settling velocity causes a shift in the entire PDF (by w_s), compared to the resolved fluid velocities. Another, but smaller, shift occurs when including the resolved acceleration term. The important point here is that the resolved acceleration term causes mostly a shift of the entire PDF, without altering its shape much. Therefore, in simplified models it may be possible to account for these changes by increasing the value for the settling velocity. It is possible that one may also need to increase the effective diffusion velocity. In order to directly quantify the effects of the resolved acceleration term in the mean concentration plume, additional results are presented in figures 6 and 7(*a*) using small filled symbols for the two γ values considered. The effects on the scaled vertical concentration profiles (figure 6) can be seen to be rather small, essentially lowering the values in the first vertical grid point and being rather negligible above that. As shown in figure 7(*a*), some small effects can be observed in the growth of the concentration boundary layer

height. They are typically about 5 % and less than the differences between the LES and the theoretical similarity solution.

4. Effect of source field size on downstream deposition

A quantity of significant interest in most applications is the ground deposition downwind from the source (or related quantities such as the amount of pollen airborne at a given distance from the source). As summarized in § 1, understanding the effect of the source field size on the dispersion patterns downwind is critical in studies of gene flow (e.g. see Timmons *et al.* 1995; Ramsay 2005). Clear effects of field size on dispersal patterns have been shown by the simplified empirical models that explicitly account for the source size (Walklate *et al.* 2004; Shaw *et al.* 2006). The assumption that airborne concentration depends on the distance from the source through an inverse square power-law leads to the conclusion that dispersal distance scales linearly with the size of the source (Shaw *et al.* 2006). However, results from these simplified models are very sensitive to the shape of the deposition function assumed (in this case an inverse power-law) and to the fitted parameters (in this case the exponent 2), which usually contain large margins of errors. In this section we use the numerical simulations presented above to investigate the validity of the arguments presented in § 2.5 and to characterize the effect of the source field size on patterns of pollen particle deposition downstream of a field.

As mentioned earlier, due to the parabolic nature of the boundary layer equation (2.5), the concentration field downwind from the source can be solved as an initial value problem, with initial condition specified by the concentration profile at the trailing edge $\overline{C}(x = L, z)$. The working hypothesis is that if the size of the field emitting pollen changes but everything else remains constant, the changes in deposition can be fully characterized by the concentration profile at the trailing edge. In addition, based on the framework presented above, $\overline{C}(x = L, z)$ can be written in terms of $\overline{C}_{max}(x = L)$, $\delta_c(x = L)$, and $g(\eta, \gamma)$. Above the source field, the maximum concentration is the one imposed as boundary condition $\overline{C}_{max}(x = L) = \overline{C}_0$. Finally, since all conditions are kept constant except for the size of the source field L, the similarity function is also expected to be the same and the changes in deposition produced by a change in field size should be fully characterized by the height of the pollen concentration boundary layer at the trailing edge $\delta_L = \delta_c(x = L) = \delta_c(\xi = 0)$. Note that this argument is consistent with (2.41). Next, the validity of these argument is verified using LES results.

In the numerical simulations, deposition fluxes are modelled through the lower boundary condition (3.3). Figure 10(*a*) shows the decay of deposition flux $\Phi(\xi)$ with distance from the trailing edge of the field ξ for the four field sizes considered. Deposition fluxes are normalized by $\overline{C}_0 u_*$, which is held constant and does not affect the relationship between deposition fluxes for the different field sizes. As first suggested by the experimental observations of Timmons *et al.* (1995) in the context of pollen flow, the decay is slower for larger field sizes, implying an increase in pollen transport far from the source field. Figure 10(*b*) presents the same curves if the scaling proposed by Shaw *et al.* (2006) is adopted. That is to say, if the dispersion patterns are linearly proportional to the size of the field L, the deposition fluxes should collapse when plotted against ξ/L. It is clear that, at least for neutral temperature stratification, there is no collapse. Instead, figure 10(*c*) presents the fluxes plotted against ξ/δ_L as suggested by our theory. In this plot, the data show good collapse for each value of γ, confirming the validity of the arguments presented above.
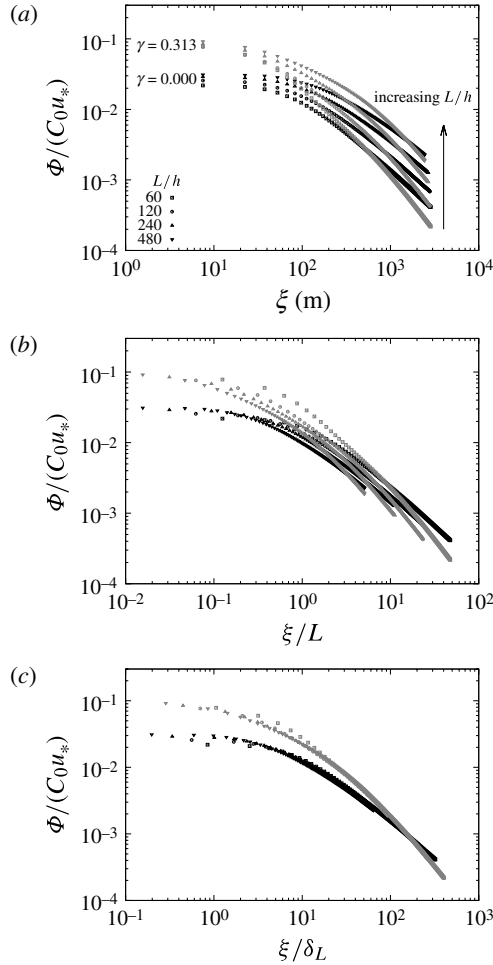
FIGURE 10. Average deposition flux as a function of distance from the trailing edge of the field for different field sizes for $\gamma = 0$ (black symbols) and $\gamma = 0.313$ (grey symbols). *x*-axis normalized following three assumptions: (*a*) that the field size has no effect on dispersion, (*b*) that scaling is proportional to field size L, and (*c*) that scaling is proportional to boundary layer height at trailing edge δ_L.

Finally, we use the deposition fluxes obtained from the LES to determine the unknown coefficients in expression (2.41). This is done by using the mass conservation constraint (2.45) to eliminate the unknown $a(\gamma)$ and write (2.41) as

$$\Phi(\xi) = \frac{F_T(\beta - 1)}{b\delta_L} \left[1 + \frac{1}{b} \frac{\xi}{\delta_L} \right]^{-\beta}. \tag{4.1}$$

Expression (4.1) provides much information about the patterns of deposition. (i) The deposition flux is directly proportional to F_T/δ_L, but since F_T is proportional to δ_L (see (2.44)), the prefactor that determines the magnitude of the deposition fluxes does not depend on the size of the source field (as shown in figure 10*c* – except for a weak dependence via η_0 in the calculation of F_T). (ii) In the near field, characterized by $\xi/\delta_L \ll b$, the deposition has a very weak dependence on the distance and asymptotes
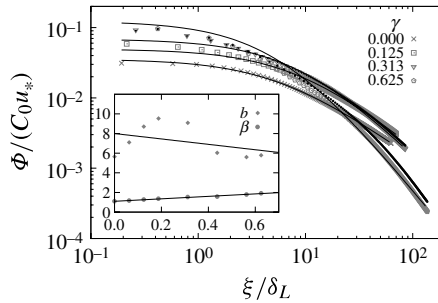
FIGURE 11. Average deposition flux as a function of normalized distance from the trailing edge of the field for different values of γ: LES results (grey symbols) and fitted solution (solid lines). The inset shows the fitted functions $b(\gamma)$ and $\beta(\gamma)$. Small black symbols indicate simulations discussed in § 3.3.

to a constant value given by the prefactor in (4.1). (iii) In the far field, given by $\xi/\delta_L \gg b$, the deposition flux presents a power-law decay with exponent $-\beta$. (iv) The transition between the two regions is controlled by the value of b, which is a function of the parameter γ. This behaviour is illustrated in the deposition flux from LES shown with grey symbols in figure 11 for four values of γ. The simulation results suggest that the power-law exponent is increasing with γ, so the decay is faster for heavier particles as expected. However, the prefactor is also larger for larger γ, indicating stronger deposition at the field's edge for heavier particles. As a consequence of these two trends, we observe a 'crossing' of the deposition curves (bear in mind that the total amount of pollen crossing the trailing edge is different for each value of γ as illustrated in figure 8).

Next we determine the functions $b(\gamma)$ and $\beta(\gamma)$ using the LES results. For each value of γ, the parameters b and β are chosen to minimize the normalized mean-squared error between (4.1) and the LES results using the simplex search algorithm of Lagarias *et al.* (1998) available in MATLAB. The resulting curves are shown together with the LES results in figure 11. The agreement is very good for low values of γ. We found that for large γ, expression (4.1) can reproduce well either the near field or the far field and will deviate from LES results in the other end. In order to capture the correct power-law decay, we choose to have better agreement in the far field (better agreement in the near field is obtained by minimizing the non-normalized mean-squared error).

In order to provide a final expression for the deposition flux, linear polynomials were fitted to the two parameters $b(\gamma)$ and $\beta(\gamma)$. The fits are shown in the inset in figure 11 and the resulting expressions are given by

$$b(\gamma) = -2.75\gamma + 8.0, \quad \beta(\gamma) = 1.25\gamma + 1.1. \tag{4.2}$$

To illustrate the applicability of the theoretical framework developed here to practical problems in pollen dispersion, we investigate the effects of γ on the distance required for the deposition flux to drop below a given threshold value Φ_t. We call this the 'isolation distance' ID_t, which is defined as the value of ξ so that $\Phi/(u_*\overline{C}_0) = \Phi_t$. Theoretical predictions of deposition flux as a function of ξ/δ_L are shown for four values of γ in figure 12(a), together with horizontal lines representing two values of Φ_t. In this plot, the normalized isolation distance for each pair (γ, Φ_t) is given by the crossing between the corresponding deposition flux and horizontal line Φ_t. The normalized isolation distances corresponding to four threshold values are shown as a
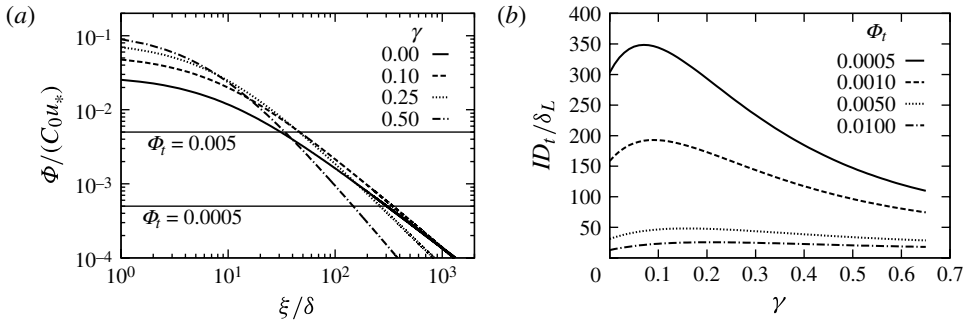
FIGURE 12. (*a*) Theoretical deposition flux as a function of normalized distance from the trailing edge of the field for different values of γ (horizontal lines represent two threshold values Φ_t). (*b*) Normalized isolation distance for the deposition flux to drop below several threshold values as a function of γ.

function of γ in figure 12(*b*). The striking feature of figure 12(*b*) is the fact that the value of ID_t/δ_L does not decrease monotonically. This feature can be understood in terms of the crossing of the deposition flux curves discussed above and illustrated in figure 12(*a*).

It is interesting to note that for a reasonable threshold (e.g. $\Phi_t = \Phi/(u_*\overline{C}_0) = 10^{-3}$ shown in dashed lines in figure 12*b*), the isolation distances can be quite large when large source fields are considered. As an example, for $\Phi_t = 10^{-3}$ and a moderate value of $\gamma = 0.3$ we have $ID_t/\delta_L \approx 150$. For a source field of length 500 m, (2.24) yields $\delta_L \approx 30$ m, corresponding to a rather long isolation distance of $ID_t \approx 4.5$ km. The value of $\gamma = 0.3$ could be relevant for pollen particles of $d_p = 55$ μm on a windy day ($u_* = 0.4$ m s^{-1}) or $d_p = 25$ μm on a calm day ($u_* = 0.1$ m s^{-1}) assuming laminar flow settling velocity, or it could correspond to even smaller particles for which larger settling velocities are assumed to hold due to increased effective settling velocity due to turbulence.

Finally, the effect of resolved flow accelerations considered in § 3.3 on the deposition patterns is quantified by showing the corresponding results for the two cases, $\gamma = 0.313$ and $\gamma = 0.625$, using small filled symbols in figure 11. It appears that for $\gamma = 0.313$ the effect is quite small. However, for the heavier particles ($\gamma = 0.625$), it is interesting to note that in the far field, there is a noticeable effect of particle inertia and interaction with turbulence in the deposition distribution. We conclude that for the heavier particles, inclusion of turbulence effects on settling velocities cannot be neglected in such simulations. Also, the results suggest that the effects of subgrid-scale accelerations may be important. Clearly, there is a need to develop subgrid models for acceleration to properly represent turbulence and subgrid-scale acceleration effects in LES of pollen transport. We point out that in recent years there have been developments of such models mostly in the context of Lagrangian models (Vinkovic *et al.* 2006; Berrouk *et al.* 2006). Shotorban & Balachandar (2007) proposed an SGS model to be used in Eulerian simulations of resolved concentration fields, which is an extension of the dynamic Smagorinsky model. However, physically based models that incorporate the effects of SGS particle velocity on resolved concentrations are still lacking.

5. Conclusions

This work presents a theoretical framework for the study of dispersion of particles released from area sources within a turbulent boundary layer. Under the assumption that particle motion is governed by fluid velocity and an effective gravitational settling velocity, the mean particle concentration field above the source field is obtained using boundary layer approximations. An analytical prediction of the mean concentration profiles as a function of normalized height is obtained, and the dependence on the settling velocity is captured. Consistent with the theoretical analysis, a suite of three-dimensional large-eddy simulations shows that mean concentration profiles exhibit self-similarity when normalized by local scales. The theoretical predictions obtained from boundary layer theory display good agreement with results from the large-eddy simulations. Both the shape of the profiles and the growth of the concentration boundary layer are shown to depend on the dimensionless parameter $\gamma = Sc w_s / \kappa u_*$, representing the ratio between gravitational settling and turbulent diffusion.

Theoretical arguments also yield expressions to predict important quantities at the trailing edge of the field: (i) the height of the particle concentration boundary layer and (ii) the total number of particles crossing being transported downstream of the field. The former is shown to be the relevant parameter to scale the effects of the source field size on the deposition patterns and the latter is a characterization of the effective particle source (i.e. the portion of the total amount emitted that is transported downstream).

Boundary layer arguments applied to the mean concentration field downstream of the source field lead to a prediction of the shape of the deposition flux onto the bottom surface as a function of distance from the source. Predictions from the numerical simulations are used to determine unknown coefficients and provide a final expression for the deposition flux. In addition, the effects of particle acceleration on the settling velocity have been explored by including a new term in the LES. Some effects were found in the far-field deposition distribution, especially for the heavier particles. The results highlighted the need for further research on subgrid-scale models for Eulerian treatments of particle concentration.

The framework presented here and the results from the LES have the potential to improve our understanding of dispersion from area sources in the atmospheric boundary layer. In practical applications, area sources are finite in the cross-stream direction and results in the far field ($\xi \gg L$) are expected to be affected by the finite size of the emitter field. Discussion of these consequences will be presented elsewhere.

REFERENCES

AHMED, A. M. & ELGHOBASHI, S. 2000 On the mechanisms of modifying the structure of turbulent homogeneous shear flows by dispersed particles. *Phys. Fluids* **12**, 1–25.

ALISEDA, A., CARTELLIER, A., HAINAUX, F. & LASHERAS, J. C. 2002 Effect of preferential concentration on the settling velocity of heavy particles in homogeneous isotropic turbulence. *J. Fluid Mech.* **468**, 77–105.

ARRITT, R. W., CLARK, C. A., GOGGI, A. S., SANCHEZ, H. L., WESTGATE, M. E. & RIESE, J. M. 2007 Lagrangian numerical simulations of canopy air flow effects on maize pollen dispersal. *Field Crops Res.* **102**, 151–162.

AYLOR, D. E. 2002 Settling speed of corn (*Zea mays*) pollen. *J. Aerosol Sci.* **33**, 1601–1607.

BERROUK, A. S., LAURENCE, D., RILEY, J. J. & STOCK, D. E. 2006 Stochastic modelling of inertial particle dispersion by subgrid motion for LES of high Reynolds number pipe flow. *J. Turbul.* **8**, 1–20.

BOU-ZEID, E., MENEVEAU, C. & PARLANGE, M. B. 2004 Large-eddy simulation of neutral atmospheric boundary layer flow over heterogeneous surfaces: blending height and effective surface roughness. *Water Resour. Res.* **40** (2), W02505.

BOU-ZEID, E., MENEVEAU, C. & PARLANGE, M. B. 2005 A scale-dependent Lagrangian dynamic model for large eddy simulation of complex turbulent flows. *Phys. Fluids* **17** (2), 025105.

BOUVET, T. & WILSON, J. D. 2006 An approximate analytical solution for the deposition of heavy particles released from an elevated line source. *Boundary-Layer Meteorol.* **119**, 1–18.

BROOKE, J. W., KONTOMARIS, K., HANRATTY, T. J. & MCLAUGHLIN, J. B. 1992 Turbulent deposition and trapping of aerosols at a wall. *Phys. Fluids* A **4**, 825–834.

BRUTSAERT, W. 1982 *Evaporation into the Atmosphere*. Reidel.

CALDER, K. L. 1949 Eddy diffusion and evaporation in flow over aerodynamically smooth and rough surfaces: a treatment based on laboratory laws of turbulent flow with special reference to conditions in the lower atmosphere. *Q. J. Mech. Appl. Math.* **2**, 153–176.

CHAMBERLAIN, A. C. 1967 Transport of *Lycopodium* spores and other small particles to rough surfaces. *Proc. R. Soc. Lond.* A **296**, 45–70.

CHAMECKI, M., VAN HOUT, R., MENEVEAU, C. & PARLANGE, M. B. 2007 Concentration profiles of particles settling in the neutral and stratified atmospheric boundary layer. *Boundary-Layer Meteorol.* **125** (1), 25–38.

CHAMECKI, M., MENEVEAU, C. & PARLANGE, M. B. 2008 A hybrid spectral/finite-volume algorithm for large-eddy simulation of scalars in the atmospheric boundary layer. *Boundary-Layer Meteorol.* **128** (3), 473–484.

CHAMECKI, M., MENEVEAU, C. & PARLANGE, M. B. 2009 Large eddy simulation of pollen transport in the atmospheric boundary layer. *J. Aerosol Sci.* **40** (3), 241–255.

CHOU, Y.-J. & FRINGER, O. B. 2008 Modeling dilute sediment suspension using large-eddy simulation with a dynamic mixed model. *Phys. Fluids* **20**, 115103.

COLEMAN, S. W. & VASSILICOS, J. C. 2009 A unified sweep-stick mechanism to explain particle clustering in two- and three-dimensional homogeneous, isotropic turbulence. *Phys. Fluids* **21**, 113301.

DUPONT, S., BRUNET, Y. & JAROSZ, N. 2006 Eulerian modelling of pollen dispersal over heterogeneous vegetation canopies. *Agric. Forest Meteorol.* **141**, 82–104.

ELGHOBASHI, S. 1994 On predicting particle-laden turbulent flows. *Appl. Sci. Res.* **52**, 309–329.

FROST, R. 1946 Turbulence and diffusion in the lower atmosphere. *Proc. R. Soc. Lond.* A **186**, 20–35.

GARRATT, J. R. 1994 *The Atmospheric Boundary Layer*. Cambridge University Press.

GASKELL, P. H. & LAU, A. K. C. 1988 Curvature-compensated convective transport: SMART, a new boundedness-preserving transport algorithm. *Intl J. Numer. Meth. Fluids* **8**, 617–641.

GERMANO, M., PIOMELLI, U., MOIN, P. & CABOT, W. H. 1991 A dynamic subgrid-scale eddy viscosity model. *Phys. Fluids* A **3** (7), 1760–1765.

GODSON, W. L. 1957 The diffusion of particulate matter from an elevated source. *Archiv für Meteorologie, Geophysik und Bioklimatologie* A **10**, 305–327.

GREGORY, P. H. 1973 *Microbiology of the Atmosphere*, 2nd edn. Wiley.

HARTEL, C., MEIBURG, E. & NECKER, F. 2000 Analysis and direct numerical simulation of the flow at a gravity-current head. Part 1. Flow topology and front speed for slip and no-slip boundaries. *J. Fluid Mech.* **418**, 189–212.

HONNAY, O., JACQUEMYN, H., BOSSUYT, B. & HERMY, M. 2005 Forest fragmentation effects on patch occupancy and population viability of herbaceous plant species. *New Phytol.* **166** (3), 723–736.

VAN HOUT, R., CHAMECKI, M., BRUSH, G., KATZ, J. & PARLANGE, M. B. 2008 The influence of local meteorological conditions on the circadian rhythm of corn (*Zea mays L.*) pollen emission. *Agric. Forest Meteorol.* **148**, 1078–1092.

JAROSZ, N., LOUBET, B., DURAND, B., MCCARTNEY, A., FOUEILLASSAR, X. & HUBER, L. 2003 Field measurements of airborne concentration and deposition rate of maize pollen. *Agric. Forest Meteorol.* **119**, 37–51.

JAROSZ, N., LOUBET, B. & HUBER, L. 2004 Modelling airborne concentration and deposition rate of maize pollen. *Atmos. Environ.* **38**, 5555–5566.

KADER, B. A. & YAGLOM, A. M. 1972 Heat and mass transfer laws for fully turbulent wall flows. *Intl J. Heat Mass Transfer* **15**, 2329–2351.

KAFTORI, D., HETSRONI, G. & BANERJEE, S. 1995 Particle behaviour in the turbulent boundary layer. Part I. Motion, deposition, and entrainment. *Phys. Fluids* **7**, 1107–1121.

KAIMAL, J. C. & FINNIGAN, J. J. 1994 *Atmospheric Boundary Layer Flows: Their Structure and Measurement.* Oxford University Press.

KIGER, K. T. & LASHERAS, J. C. 1997 Dissipation due to particle/turbulence interaction in a two-phase, turbulent, shear layer. *Phys. Fluids* **3005**, 1–19.

KIND, R. J. 1992 One-dimensional aeolian suspension above beds of loose particles: a new concentration-profile equation. *Atmos. Environ.* A **26** (5), 927–931.

KLEIN, E. K., LAVIGNE, C., FOUEILLASSAR, X., GOUYON, P. H. & LARÉDO, C. 2003 Corn pollen dispersal: quasi-mechanistic models and field experiments. *Ecol. Monogr.* **73**, 131–150.

LAGARIAS, J. C., REEDS, J. A., WRIGHT, M. H. & WRIGHT, P. E. 1998 Convergence properties of the Nelder–Mead simplex method in low dimensions. *SIAM J. Optim.* **9** (1), 112–147.

LEHNING, M., LÖWE, H., RYSER, M. & RADERSCHALL, N. 2008 Inhomogeneous precipitation distribution and snow transport in steep terrain. *Water Resour. Res.* **44**, W07404.

MARCHIOLI, C. & SOLDATI, A. 2002 Mechanisms for particle transfer and segregation in a turbulent boundary layer. *J. Fluid Mech.* **468**, 283–315.

MARTIN, M., CHAMECKI, M. & BRUSH, G. S. 2010 Anthesis synchronization and floral morphology determine diurnal patterns of ragweed pollen dispersal. *Agric. Forest Meteorol.* **150**, 1307–1317.

MAXEY, M. R. 1987 The gravitational settling of aerosol particles in homogeneous turbulence and random flow fields. *J. Fluid Mech.* **174**, 441–465.

MAXEY, M. R. & RILEY, J. J. 1983 Equation of motion for a small rigid sphere in a nonuniform flow. *Phys. Fluids* **26** (4), 883–889.

MCCARTNEY, H. A. & LACEY, M. E. 1991 Wind dispersal of pollen from crops of oilseed rape (*Brassica napus L.*). *J. Aerosol Sci.* **22** (4), 467–477.

MCLAUGHLIN, J. B. 1989 Aerosol particle deposition in numerically simulated channel flow. *Phys. Fluids* A **1**, 1210–1224.

MENEVEAU, C., LUND, T. S. & CABOT, W. H. 1996 A Lagrangian dynamic subgrid-scale model of turbulence. *J. Fluid Mech.* **319**, 353–385.

MESSEGUER, J. 2003 Gene flow assessment in transgenic plants. *Plant Cell, Tissue and Organ Culture* **73**, 201–212.

NECKER, F., HAERTEL, C., KLEISER, L. & MEIBURG, E. 2002 High-resolution simulations of particle-driven gravity currents. *Intl J. Multiphase Flow* **28**, 279–300.

NECKER, F., HAERTEL, C., KLEISER, L. & MEIBURG, E. 2005 Mixing and dissipation in particle-driven gravity currents. *J. Fluid Mech.* **545**, 339–372.

O'CONNELL, L. M., MOSSELER, A. & RAJORA, O. P. 2007 Extensive long-distance pollen dispersal in a fragmented landscape maintains genetic diversity in white spruce. *J. Heredity* **98**, 640–645.

PEDINOTTI, S., MARIOTTI, G. & BANERJEE, S. 1992 Direct numerical simulation of particle behaviour in the wall region of turbulent flows in horizontal channels. *Intl J. Multiphase Flow* **18**, 927–941.

PHILIP, J. R. 1959 The theory of local advection. Part I. *J. Atmos. Sci.* **16**, 535–547.

PRANDTL, L. 1952 *Essentials of Fluid Dynamics.* Blackie.

RAMSAY, G. 2005 Pollen dispersal vectored by wind or insects. In *Gene Flow from GM Plants* (ed. G. M. Poppy & M. J. Wilkinson), chap. 5, pp. 43–73. Blackwell.

RASHIDI, M., HETSRONI, G. & BANERJEE, S. 1990 Particle-turbulence interaction in a boundary layer. *Intl J. Multiphase Flow* **16**, 935–949.

RAYNOR, G. S., OGDEN, E. C. & HAYES, J. V. 1972*a* Dispersion and deposition of timothy pollen from experimental sources. *Agric. Meteorol.* **9**, 347–366.

RAYNOR, G. S., OGDEN, E. C. & HAYES, J. V. 1970 Dispersion and deposition of ragweed pollen from experimental sources. *J. Appl. Meteorol.* **9** (6), 885–895.

RAYNOR, G. S., OGDEN, E. C. & HAYES, J. V. 1972*b* Dispersion and deposition of corn pollen from experimental sources. *Agronomy J.* **64**, 420–427.

REEKS, M. W. 1983 The transport of discrete particles in inhomogeneous turbulence. *J. Aerosol Sci.* **14**, 729–739.

ROUNDS, W. 1955 Solutions of the two-dimensional diffusion equations. *Trans. Am. Geophys. U.* **36**, 395–405.

ROUSE, H. 1937 Modern conceptions of the mechanics of fluid turbulence. *Trans. ASCE* **102**, 463–505.

ROUSON, D. W. I. & EATON, J. K. 2001 On the preferential concentration of solid particles in turbulent channel flow. *J. Fluid Mech.* **428**, 149–169.

SHAW, M. W., HARWOOD, T. D., WILKINSON, M. J. & ELLIOTT, L. 2006 Assembling spatially explicit landscape models of pollen and spore dispersal by wind for risk assessment. *Proc. R. Soc. Lond.* B **273**, 1705–1713.

SHOTORBAN, B. & BALACHANDAR, S. 2007 A Eulerian model for large-eddy simulation of concentration particles with small Stokes numbers. *Phys. Fluids* **19**, 118107.

SMITH, D. M. 2001 Algorithm 814: Fortran 90 software for floating-point multiple precision arithmetic, gamma and related functions. *ACM Trans. Math. Softw.* **27**, 377–387.

SNYDER, W. H. & LUMLEY, J. L. 1971 Some measurements of particle velocity autocorrection functions in a turbulent flow. *J. Fluid Mech.* **48**, 41–47.

SORK, V. L. & SMOUSE, P. E. 2006 Genetic analysis of landscape connectivity in tree populations. *Landscape Ecol.* **21**, 821–836.

SQUIRES, K. D. & EATON, J. K. 1991 Preferential concentration of particles by turbulence. *Phys. Fluids* A **3**, 1169–1178.

SUTTON, O. G. 1934 Wind structure and evaporation in a turbulent atmosphere. *Proc. R. Soc. Lond.* A **146**, 701–722.

TIMMONS, A. M., O'BRIEN, E. T., CHARTERS, Y. M., DUBBELS, S. J. & WILKINSON, M. J. 1995 Assessing the risks of wind pollination from fields of genetically modified *Brassica napus ssp. oleifera*. *Euphytica* **85**, 417–423.

VINKOVIC, I., AGUIRRE, C., SIMOENS, S. & GOROKHOVSKI, M. 2006 Large eddy simulation of droplet dispersion for inhomogeneous turbulent wall flow. *Intl J. Multiphase Flow* **32**, 344–364.

WALKLATE, P. J., HUNT, J. C. R., HIGSON, H. L. & SWEET, J. B. 2004 A model of pollen-mediated gene flow for oilseed rape. *Proc. R. Soc. Lond.* B **271**, 441–449.

WANG, L. P. & MAXEY, M. R. 1993 Settling velocity and concentration of heavy particles in homogeneous isotropic turbulence. *J. Fluid Mech.* **256**, 27–68.

YEH, G.-T. & BRUTSAERT, W. 1970 Perturbation solution of an equation of atmospheric turbulent diffusion. *J. Geophys. Res.* **75**, 5173–5178.

ZEDLER, E. A. & STREET, R. L. 2001 Large-eddy simulation of sediment transport: currents over ripples. *J. Hydraul. Engng* **127** (6), 444–452.